Available online at www.keaipublishing.com/en/journals/journal-of-magnesium-and-alloys/

ScienceDirect

Journal of Magnesium and Alloys 13 (2025) 3751–3767

www.elsevier.com/locate/jma

Full Length Article

Research on edge defects suppression of Mg/Al composite plate rolling: Development of embedded rolling technology ☆

Chenchen Zhao [a,e], Zhiquan Huang [b,*], Haoran Zhang [c,e], Peng Li [c,e], Tao Wang [c,d,e], Qingxue Huang [a,c,e]

[a] School of Mechatronics Engineering, Harbin Institute of Technology, Harbin, 150006, China
[b] School of Materials Science and Engineering, Taiyuan University of Science and Technology, Taiyuan 030024, China
[c] College of Mechanical and Vehicle Engineering, Taiyuan University of Technology, Taiyuan, 030024, China
[d] National Key Laboratory of Metal Forming Technology and Heavy Equipment, Xi'an, 710000, China
[e] Engineering Research Center of Advanced Metal Composites Forming Technology and Equipment, Ministry of Education, Taiyuan, 030024, China

Received 23 July 2024; received in revised form 11 November 2024; accepted 18 November 2024
Available online 10 December 2024

Abstract

Edge defects significantly impact the forming quality of Mg/Al composite plates during the rolling process. This study aims to develop an effective rolling technique to suppress these defects. First, an enhanced Lemaitre damage model with a generalized stress state damage prediction mechanism was used to evaluate the key mechanical factors contributing to defect formation. Based on this evaluation, an embedded composite rolling technique was proposed. Subsequently, comparative validation was conducted at 350 °C with a 50% reduction ratio. Results showed that the plates rolled using the embedded composite rolling technique had smooth surfaces and edges, with no macroscopic cracks observed. Numerical simulation indicated that, compared to conventional processes, the proposed technique reduced the maximum edge stress triaxiality of the plates from −0.02 to −1.56, significantly enhancing the triaxial compressive stress effect at the edges, which suppressed void nucleation and growth, leading to a 96% reduction in damage values. Mechanical property evaluations demonstrated that, compared to the conventional rolling process, the proposed technique improved edge bonding strength and tensile strength by approximately 67.7% and 118%, respectively. Further microstructural characterization revealed that the proposed technique, influenced by the restriction of deformation along the transverse direction (TD), weakened the plastic flow in the TD and enhanced plastic flow along the rolling direction (RD), resulting in higher grain boundary density and stronger basal texture. This, in turn, improved the toughness and transverse homogeneity of the plates. In summary, the embedded composite rolling technique provides crucial technical guidance for the preparation of Mg-based composite plates.

Keywords: Numerical simulation; Damage model; Stress triaxiality; Mg/Al composite plate; Embedded composite rolling.

1. Introduction

Laminated metal composites have garnered increasing attention due to their ability to leverage the advantages of heterogeneous constituent metals [1,2]. One such composite, the Mg/Al composite plate, integrating the low density and high strength of magnesium (Mg) alloys with the superior corrosion resistance of aluminum (Al) alloys, emerges as a material of significant potential across diverse sectors including aerospace, medical, automotive, and electronic fields [3,4]. To achieve a composite plate with stable properties, various fabrication processes have been proposed, including explosion, extrusion, casting, and rolling et al. [5,6]. Among these, rolling, as an efficient plastic deformation technique, offers advantages such as low cost and ease of implementation, making it the predominant method for the production of Mg/Al composite plates [7].

☆ Peer review under the responsibility of Chongqing University.
* Corresponding author.
E-mail address: zhiquanhuang@tyust.edu.cn (Z. Huang).

https://doi.org/10.1016/j.jma.2024.11.024

However, conventional rolling processes often struggle to produce high-quality composite plates in actual production. The issues affecting the quality of plate forming are primarily manifested in three aspects: 1) high residual stress [8], 2) low bonding [9] strength, and 3) susceptibility of Mg alloy edges to cracking [10]. These deficiencies have become bottleneck issues that limit the large-scale application of composite plates. To enhance the quality of plate forming, several process-level improvements have been proposed. Addressing the issue of high residual stress, existing research suggests that by designing the rollers in a wave-like pattern for wave-flat rolling, coordinated deformation between layered metals can be effectively promoted during the rolling process, thereby reducing residual stress [11]. Additionally, asymmetric rolling processes [12], ultrasonic vibration-assisted friction stir welding [13], and cast rolling have been proven to effectively reduce residual stress. Regarding the issue of low bonding strength, cold spray rolling technology is considered an effective method. This technology can promote atomic diffusion on the interface, thereby increasing its bonding strength by 2.5 times [14]. Furthermore, improving the morphology or elemental composition of the bonding interface is also believed to significantly enhance bonding performance. However, so far, there has been limited progress in research on the process of suppressing edge cracking in Mg/Al composite plates.

Although the development of edge crack suppression techniques for Mg/Al composite plates has not been extensively studied, considerable scholarly effort has been dedicated to investigating the mitigation of edge cracks during the rolling process of Mg alloy plates. Indeed, higher rolling speeds [15], higher temperatures [16], and smaller reduction rates have been identified as factors that mitigate crack evolution. However, optimization of rolling parameters alone cannot address the root cause of edge defects, and more substantial improvements should be reflected at the process level. It has been demonstrated that multi-cross [17] and accumulative rolling [18] can effectively suppress edge cracks in the rolling of Mg alloy plates. Furthermore, modifications to rolling equipment, including vertical rolling [19], and width-limited rolling [20], have been proven to be effective in crack suppression. Additionally, altering the elemental composition and shape of Mg alloys has been also shown to enhance the formability [21]. Previous studies have indicated that prefabricated crown on the edges of Mg alloys facilitates metal flow along the RD. When subjected to multiple rolling passes at 400 °C, this modification resulted in a 77% reduction in the incidence of edge cracks [22]. The emergence of these novel processes offers multiple solutions for improving the formability of Mg alloy plates. However, the applicability of these processes developed for Mg alloy plates to Mg/Al composite plates remains to be evaluated.

The coupling of finite element methods with damage models has proven to be an effective strategy for guiding improvements in manufacturing processes, as evidenced by its successful application in the optimization of Mg alloy plate processes [23]. The essence of this approach lies in the selection of a suitable damage criterion to accurately predict the evolution characteristics of edge cracks. Damage models can be dichotomized into uncoupled and coupled types based on whether they are integrated with flow stress [24]. To date, uncoupled damage models have been widely adopted in various fields, including skew rolling [25], cross wedge rolling [26], spinning [27], and plastic processing techniques, due to their structural simplicity and ease of implementation. However, these models exhibit limitations in predicting crack propagation, thus hindering their utility in guiding process improvements [28]. In contrast, coupled damage models, typically derived from thermodynamics or micromechanics of metals, incorporate a broader range of physical phenomena, making them more suitable for analyzing the causes of damage evolution. Nevertheless, classical damage models, including the widely utilized the Lemaitre model [29] and Gurson-Tvergaard-Needleman (GTN) model [30], exhibit limitations in accurately representing the nucleation mechanisms of voids dominated by shear in forming processes under pressure [31–33]. Moreover, the complexity of stress states and interface contact issues during the rolling of composite plates pose significant challenges to the integration of these models into finite element numerical iterations. Fortunately, our previous research introduced an enhanced Lemaitre damage model tailored for compression molding processes [34]. This model accounts for damage evolution mechanisms under complex stress states and can accurately predict defect locations and morphologies during the rolling of composite plates, offering valuable technical guidance for the improvement of rolling processes.

Scientific research methods play a crucial role in enhancing manufacturing processes. Building on previously established theories of damage models and mechanisms of crack initiation, this study introduces a novel rolling technique designed to effectively mitigate edge damage in Mg/Al composite plate rolling. Employing both experimental and computational simulation, the study elucidates the underlying principles by which this novel technique suppresses edge defects. Furthermore, the research compares the formability of composite plates under two different processes, utilizing mechanical loading and microstructural characterization experiments. This proposed rolling technique offers an effective method for fabricating Mg-based composite plates.

2. Theoretical model

In our previous research, we proposed a damage model for the pressure molding of composite plates, based on the framework of the standard Lemaitre model [34]. Compared to the standard Lemaitre model [29], the enhanced Lemaitre model [34] offers several advantages, including simplicity of implementation, precise damage prediction, and the capability to forecast damage evolution under a broader range of stress states. This section first reviews the structural formulation of the damage model we previously proposed, followed by a discussion on its numerical integration and the calibration of damage parameters.

2.1. Continuum damage mechanics model

Similar to the standard Lemaitre model [29], the enhanced Lemaitre model [34] characterizes the degradation behavior of materials during the loading process at the microscopic level by defining an effective bearing area:

$$S_0{}^* = S_0 - S_D, \tag{1}$$

where $S_0{}^*$, S_0 and S_D effective bearing area, the original bearing area, and the damaged region, respectively. The damage value is delineated as the quotient of the defected region to the original bearing region,

$$D = \frac{S_D}{S_0} \text{ for } 0 \le D \le 1. \tag{2}$$

At the macroscopic scale, the stress relaxation caused by damage during the material loading process is reflected through the effective stress and effective elastic modulus,

$$\sigma_{ij} = \tilde{\sigma}_{ij}(1 - D), \tag{3}$$

$$E^* = E(1 - D), \tag{4}$$

where $\tilde{\sigma}_{ij}$ and σ_{ij} signify the effective stress tension and stress tenson, respectively. E^* and E denote the equivalent elastic modulus and conventional elastic modulus, respectively.

In the aspect of damage evolution, the non-linear progression of damage is characterized by a power function composed of the ratio of the equivalent plastic strain (EPS) and the critical fracture strain,

$$D = \left(\frac{\varepsilon_{eq}^p}{\varepsilon_f}\right)^n, \tag{5}$$

where n and ε_f represent the softening factor and critical fracture strain. This damage evolution model has been validated across some applications [35], offering two primary advantages: 1) its construction is straightforward, facilitating easy implementation; 2) the critical damage value has been normalized, obviating the need for calibrating specific damage failure thresholds. Consequently, when the damage value D attains unity, it signifies the onset of fracture behavior. A rate-dependent formulation can be deduced by Eq. (5),

$$\dot{D} = n(\varepsilon_{eq}^p)^{n-1}(\varepsilon_f)^{-n}\dot{\varepsilon}_{eq}^p. \tag{6}$$

The construction of a coupling mechanism between stress states and damage evolution serves as the foundation for achieving generalized damage prediction. To this end, the enhanced Lemaitre model [34] incorporates a concise stress state function as the denominator in the damage evolution function, effectively defining a comprehensive fracture envelope. This approach facilitates broader predictions of forming limits. The stress state function integrates the Lode parameter and stress triaxiality, as expressed by the following equation:

$$\chi(\eta, L) = \left[\frac{(1 - L^2) + 1}{2\alpha}\right]\exp\left[\frac{-\eta}{\eta + \eta_{\lim}}\right], \tag{7}$$

where α is the material parameter that can be adjusted to alter the damage evolution rate. η and L and is the stress triaxiality and Lode parameter, respectively, and their expressions delineated as follows:

$$\eta = \frac{\sigma_{eq}}{\sigma_h} = \frac{3\sqrt{3s_{ij}s_{ij}}}{\sqrt{2}tr(\sigma_{ij})} \tag{8}$$

$$L = \frac{2s_2 - s_1 - s_3}{s_1 - s_3}, \tag{9}$$

where $\eta_{\lim}$ is the critical stress triaxiality [36]. Its expression is $\eta_{\lim} = \frac{L-3}{3\sqrt{L^2+3}} - C$, where C is a material parameter. This function's significance lies in providing a cutoff value for stress triaxiality, below which the damage will cease to grow.

The enhanced Lemaitre model [34] incorporates the total equivalent plastic strain (EPS) in its damage evolution equation (Eq. (12)). However, in certain engineering applications, materials undergo frequent loading and unloading cycles due to non-unidirectional loading, leading to premature fracture predictions. To address this issue, the concept of effective equivalent plastic strain (EEPS) has been introduced into the damage evolution mechanism. The revised damage evolution equation is as follows:

$$\dot{D} = \frac{n(\varepsilon_{eq}^p{}^*)^{n-1}(\varepsilon_f)^{-n}\dot{\varepsilon}_{eq}^p{}^*}{\chi(\eta, L)} = \frac{n(\varepsilon_{eq}^p{}^*)^{n-1}(\varepsilon_f)^{-n}\dot{\varepsilon}_{eq}^p{}^*}{[\frac{(1-L^2)+1}{2\alpha}]\exp[\frac{-\eta}{\eta+\eta_{\lim}}]}, \tag{10}$$

$$\dot{\varepsilon}_{eq}^{p*} = \dot{\varepsilon}_{eq}^p(\eta > \eta_{\lim})$$
$$\dot{\varepsilon}_{eq}^{p*} = 0(\eta \le \eta_{\lim}), \tag{11}$$

where $\dot{\varepsilon}_{eq}^{p*}$ represents the rate of EEPS, which will cease to grow when the critical stress triaxiality surpasses the stress triaxiality at the material point.

2.2. Numerical implementation method

To incorporate the enhanced Lemaitre model into the finite element (FE) calculation, a crucial challenge lies in determining the correctly stress update for each incremental step. The radial return algorithm serves as a general solution to this problem [37]. This algorithm operates on the principle of operator splitting, wherein each incremental step is assumed to be elastic to obtain the trial stress. Subsequently, when the model satisfies the plastic yield condition, the discrete equation is iterated numerically to determine the plastic strain and stress components. In this study, the numerical solution of the model was performed using a fully implicit backward Euler integration scheme. This algorithm has been validated in numerous previous studies [38,39]. The specific details of the numerical algorithm utilized in this research are provided in Appendix A.

2.3. Parameters calibration method

Given that rolling as a representative pressure forming technique, Gleeble high-temperature mechanical compression tests on AZ31B Mg alloy and 5052 Al alloy can assume the stress state during rolling. By adjusting the material parameters, the simulation's mechanical response curves can be

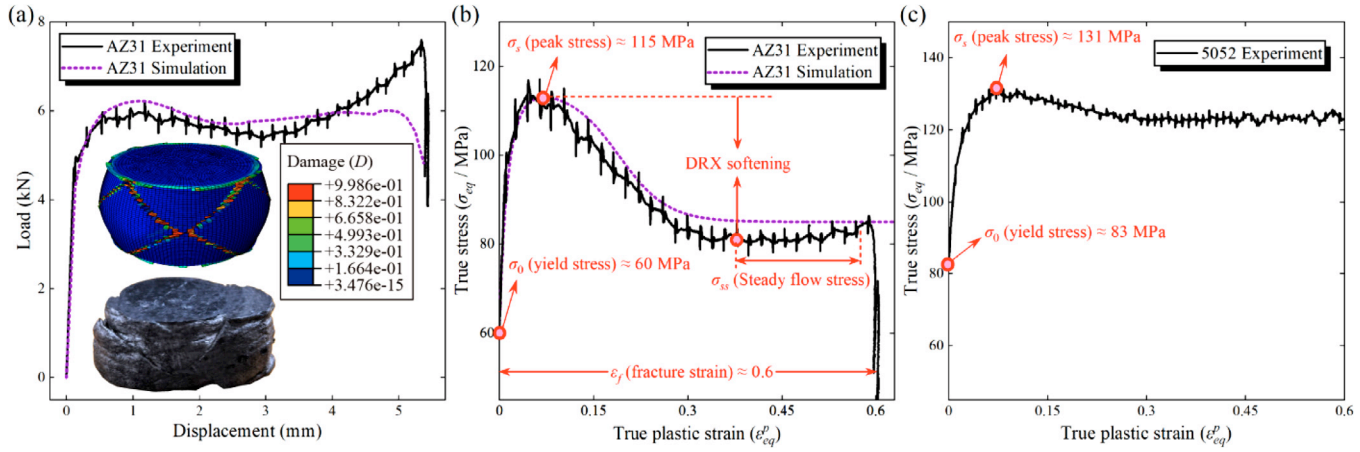

Fig. 1. Thermal compression experiments were conducted on AZ31 Mg alloy and 5052 Al alloy. The force-displacement and flow stress fitting curves for AZ31 are presented in (a) and (b), respectively, while the flow stress curve for 5052 is depicted in (c).

aligned with experimental results to ascertain the correct material parameters. Notably, within this investigation, the enhanced Lemaitre damage model is utilized for the Mg alloy, while the stress-strain behavior for the Al alloy is calculated by the internal constitutive model in Abaqus.

In terms of stress fitting, a flow stress function integrating coupled dynamic recrystallization (DRX) behavior is employed [40,41], expressed as follows:

$$\sigma_y = [\sigma_s^2 + (\sigma_0^2 - \sigma_s^2)\exp(-\Omega_\varepsilon \varepsilon_{eq}^p)]^{1/2} - (\sigma_s - \sigma_{ss})X_{DRX} \tag{12}$$

where σ_s, σ_0 and σ_{ss} denote peak stress, yield stress, and steady-state flow stress, respectively. Ω_ε is a temperature-dependent parameter. The DRX model, which is predominantly a function of EPS, is adopted in this study based on the model proposed by Liu et al. [42],

$$X_{DRX} = \left[k_v \wedge \left(1 - \frac{\varepsilon_p^{eq} - \varepsilon_c}{\varepsilon_{0.5} - \varepsilon_c}\right) + 1\right]^2, \tag{13}$$

where ε_c and $\varepsilon_{0.5}$ denote the strain at the activate of DRX and at 50% completion of DRX, respectively. k_v is a materal parameter.

Mechanical loading experiments were conducted using a Gleeble high-temperature mechanical tester, with the compression specimens having diameters and heights of 8 mm and 12 mm, respectively. The loading rate and temperature were set at 2 s^{-1} and 350 °C, respectively. In FE simulation modeling of the compression specimens, the mesh type and size were C3D8R and 0.5 mm, respectively, and the interfacial friction coefficient is set at 0.2 [43]. The final parameter fitting results are presented in Fig. 1, and the specific values of the material parameters can be found in our previous work [34].

3. Application of damage model in novel rolling technology development

This section begins by reviewing conclusions drawn from previous studies regarding the reason of edge defects during the rolling process. It then introduces a novel rolling technique designed to inhibit edge damage in composite plate rolling: the embedded composite rolling process. The final part compares the edge defect morphology and distribution in Mg alloys under both techniques, using experimental results and FE prediction.

In the FE simulation, the rolling model employed is depicted in Fig. 2. To enhance computational stability, the rolls and the plate were modeled as discrete rigid bodies and a 1/2 vol elastic body, respectively. The mesh for both the rolls and the plate was set at a granularity of 0.5 mm, with the rolls' mesh arranged circumferentially. The contact algorithms for the bonding interface and the plate-roll interaction are pre-bonding and Coulomb friction, respectively, with a friction coefficient of 0.3. To better match with the experimental procedure, the rolls' rotational speed was set at 0.6 rad/s. Additionally, the plate was assigned an initial velocity of 80 mm/s to emulate its being fed into the rolling mill entrance.

3.1. Review on causes of Mg alloy edge damage

In our previous work, we analyzed the evolution mechanism of edge cracks during Mg/Al composite plates rolling, pinpointing high stress triaxiality at the Mg alloy edges as a key contributor to edge defects [34]. This analysis is concisely reviewed below. The stress triaxiality distribution during the rolling process, illustrated in Fig. 3(a), exhibits a progressive increase from the plate's edge to its center. To more clearly illustrate the trend of stress triaxiality changes during rolling, a path from the edge element Mg_E1 to the central element Mg_C1, designated as nodes set Path 1, was defined. Fig. 3(b) presents the distribution of stress triaxiality and damage values along Path 1 at four stages of the rolling process, each stage marked by a 10% increase in deformation in the normal direction (ND) during rolling. Observations indicate that with escalating deformation, stress triaxiality in the plate's central region progressively diminishes, while the edge regions maintain a relatively high range. This discrepancy fosters conditions conducive to voids nucleation and expansion,

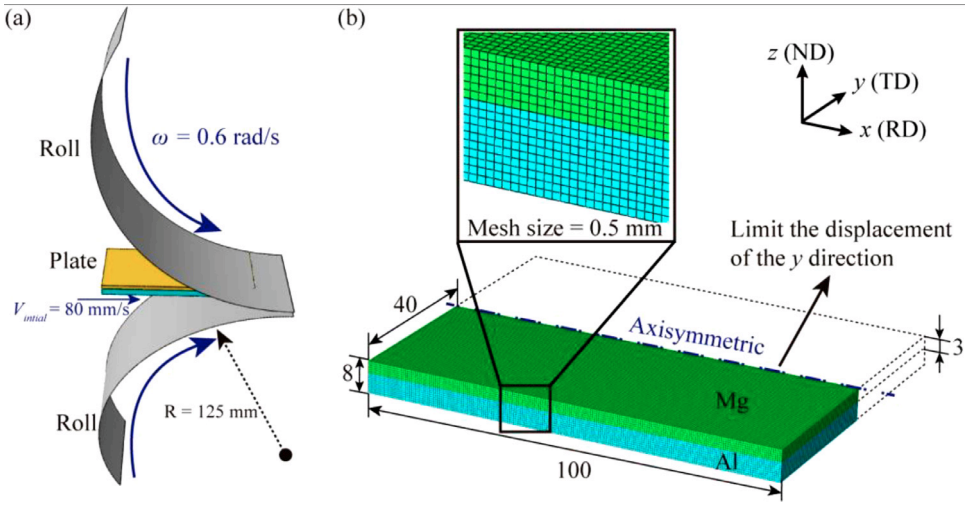

Fig. 2. The rolling FE model developed for the Mg/Al composite plate is depicted in (a), which illustrates the macroscopic modeling of the rolls and the plate. Details concerning the dimensions of the plate, and the mesh specifications are provided in (b).

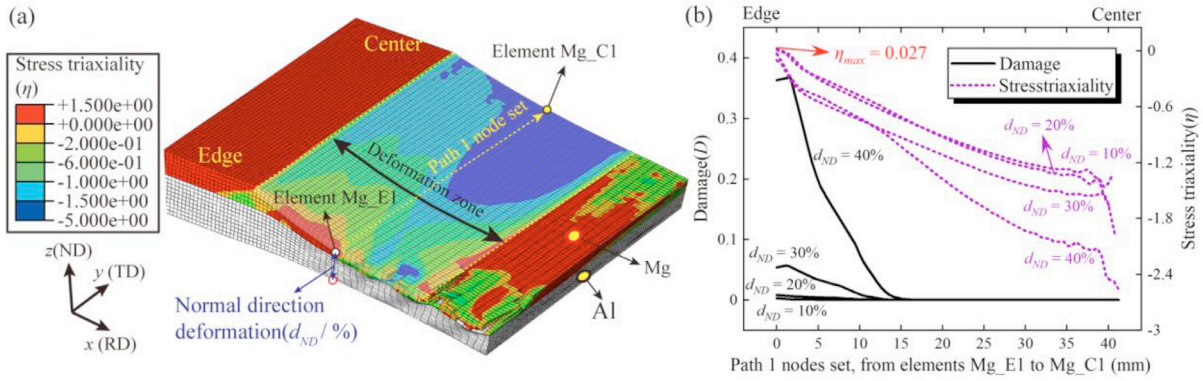

Fig. 3. Analysis of factors affecting edge defects. (a) Stress triaxiality distribution of plate during conventional rolling process. (b) The change trend of Path 1 nodes set damage value and stress triaxial degree with plate deformation along the ND.

leading to significant damage accumulation exclusively at the edges of the plate. Therefore, the focus of proposed process development is on reducing the stress triaxiality at the edges of the plate, which will be described in detail subsequently.

3.2. Development of embedded rolling technology

To mitigate the elevated stress triaxiality at the edges of the plate during the rolling process, it is essential to maintain a triaxial compressive stress state at plate edge. Consequently, a novel technique termed 'embedded composite rolling' has been proposed. As illustrated in Fig. 4, the proposed process requires slotting treatment of Al alloy with dimensions of $l \times w_1 \times h_1$. The width of the slot, denoted as 'w', is kept consistent with the width of the Mg alloy, while the depth of the slot, denoted as 'h', matches the thickness of the Mg alloy. It is important to highlight that an interference fit is employed between the Al and Mg alloys to prevent relative sliding during the rolling process. Besides, the length of w_1 is an important factor influencing the formability of the composite plate. Generally, wider composite plates (larger w) require a corresponding increase in the length of w_1. To maximize the formability of the composite plate while minimizing material consumption, a recommended size for w_1 is provided as $w_1 = 1.5\ w$.

In the rolling experiment, the initial step involves the meticulous polishing of the bonding interface of the plates, followed by binding with Al wire (this procedure exclusive to traditional process). Subsequently, the plates are placed in a furnace preheated to 350 °C for a duration of 20 min. During this annealing process, argon gas is introduced into the furnace to prevent the oxidation of the Mg alloy, after which rolling is immediately conducted.

3.3. Validation of Mg/Al embedded composite rolling process

To validate the forming effectiveness of the proposed process, rolling experiments were conducted on 5052 Al alloy and AZ31B Mg alloy. The dimensional details of the billets were as follows: $w_1 = 1.5\ w = 120$ mm, $l = 100$ mm,

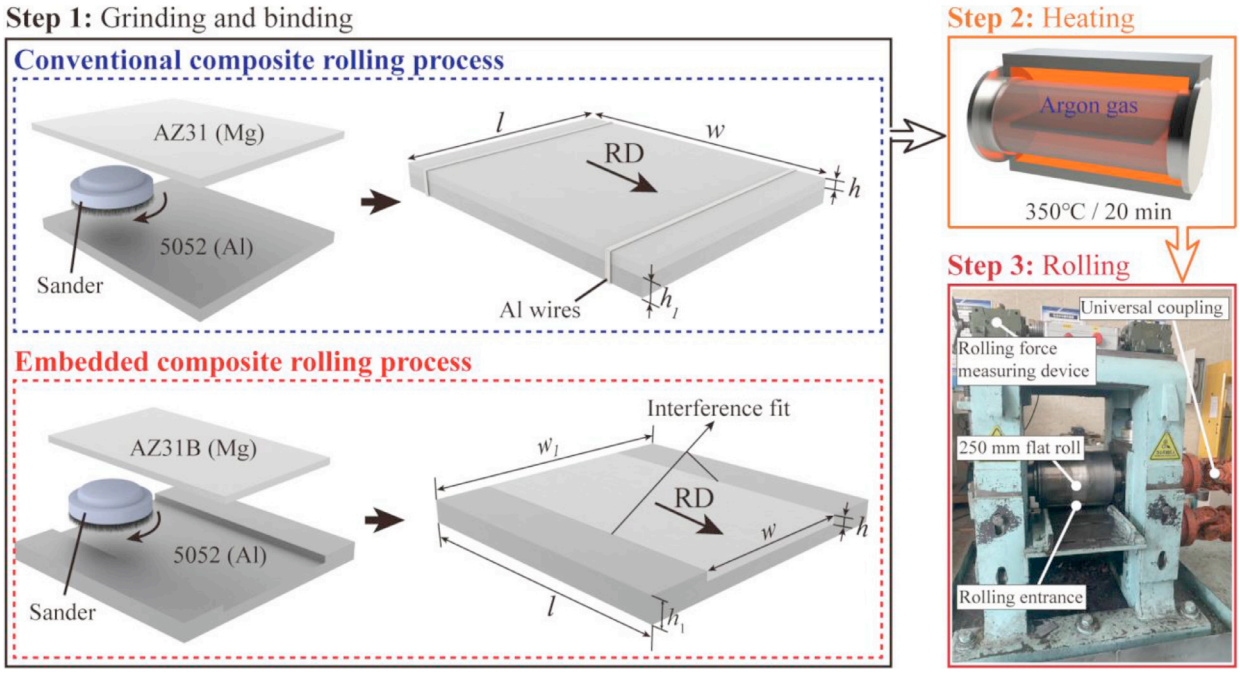

Fig. 4. The 3D diagram of conventional and embedded rolling processes and the details of billet dimensions.

$h = 3$ mm, and $h_1 = 8$ mm. Since there was an interference fit between the Mg and Al alloys, no clamping was required at the head or end of the composite plate. Furthermore, the remaining experiment and simulation parameters and plate treatment procedures were consistent with the conventional process. The enhanced Lemaitre damage model was utilized to reflect the damage distribution in the Mg/Al composite plate during the embedded composite rolling process.

Figs. 5(a) and (b) present a comparative analysis of the surface and side morphologies of Mg/Al composite plates rolled under both processes. In the conventional process, the surface exhibits significant roughness and irregularities, especially along the TD and RD. Noticeable edge cracks are present, indicating the susceptibility of the conventional process to edge damage. Additionally, the presence of edge defects has resulted in a distinct stratification between Mg and Al alloys, with the bonding interface exhibiting a wavy appearance. This suggests that the composite performance at the edges of the plate may be compromised. In contrast, the surface morphology of the plates fabricated using the proposed process is notably smoother and more uniform, with no macroscopic cracks observed. The side morphology (section *A-A*) displays a well-bonded interface between the Mg and Al layers, with smooth surface and no delamination, indicating superior bonding quality. The absence of significant cracks further underscores the effectiveness of the proposed process in mitigating edge damage.

The FE results in Figs. (c) and (d) further confirm the experimental findings. For the conventional rolling process, Fig. (c) shows extensive surface damage distribution, particularly near the edges, with a high damage value. The side damage distribution reveals a zigzag pattern of damage, corresponding to the observed experimental delamination and poor bonding. Conversely, Fig. (d) demonstrates that the embedded composite rolling process results in a significantly reduced surface damage distribution, with the maximum damage value around 0.04. The side damage distribution (section *B-B*) is more uniform and minimal, consistent with the experimental observations of improved bonding and reduced defects.

Overall, the embedded composite rolling process significantly enhances the surface and interfacial quality of Mg/Al composite plates, as evidenced by the smoother surfaces, better-bonded interfaces, and reduced edge cracks. The following section will further analyze the damage suppression mechanism of the proposed process from a mechanical perspective.

4. Analysis of damage inhibition factors and formability performance evaluation

In this section, a comparison made between the stress states and damage evolution during the rolling process under both rolling techniques, with a focus on analyzing the mechanism of edge defect suppression in the proposed process from a mechanical perspective.

4.1. Cause analysis of damage suppression under the embedded composite rolling process

Fig. 6 illustrates the distribution of mechanical variables on the nodes set of Path 1 under proposed process. It should be noted that in the discussion of this section, the location of the node set for path 1 corresponds to that shown in Fig. 3(a). In the case of a deformation amount of 20% (Fig. 6(a)), the EPS at the edges of the Mg alloy increased from 0.3 to 0.4 compared to the conventional rolling process. Moreover, a ho-

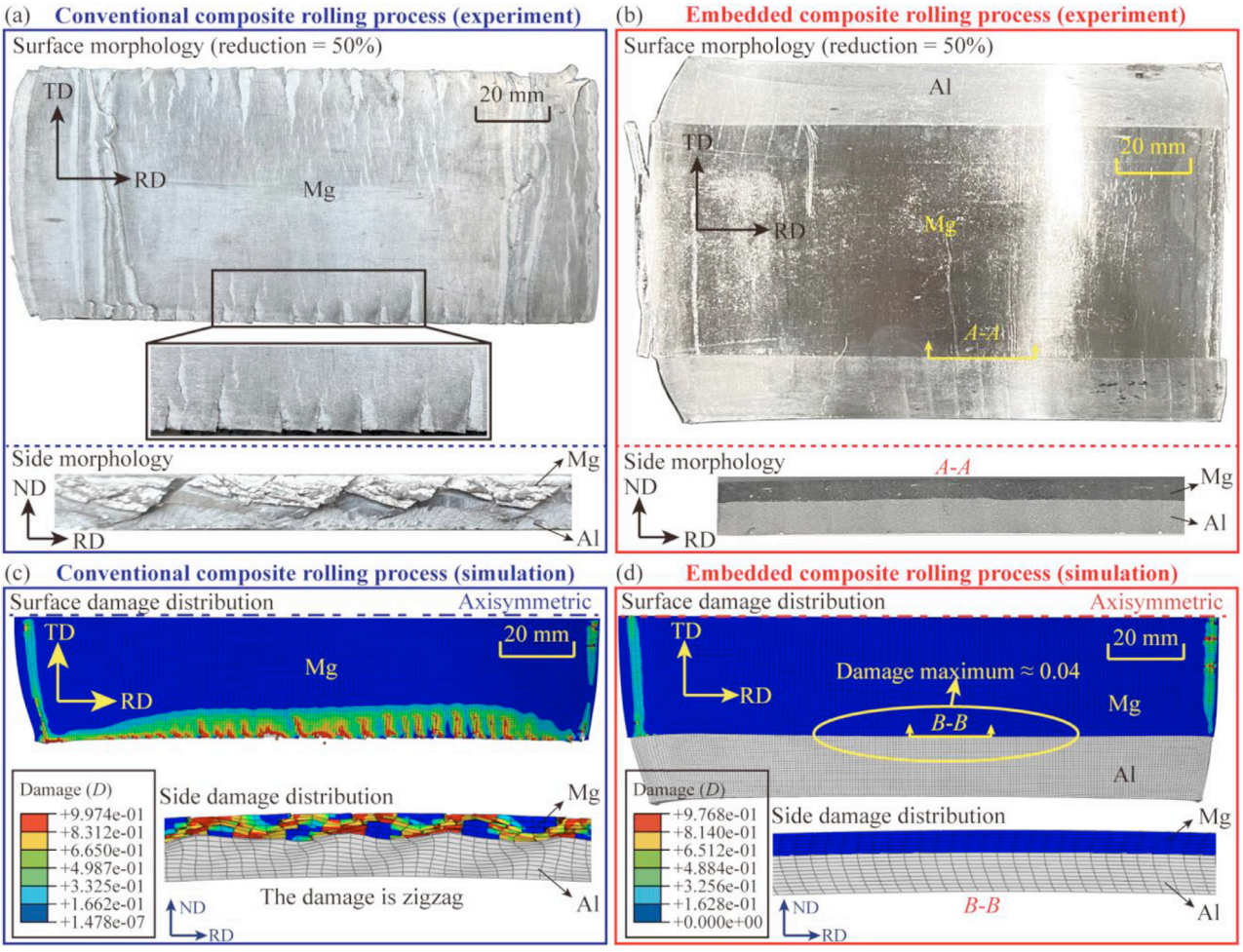

Fig. 5. The comparison of macroscopic morphology of the Mg/Al composite plates fabricated using both rolling processes, focusing on the surfaces and side views. Experimental comparisons are illustrated in (a) and (b), while simulated damage distribution are presented in (c) and (d).

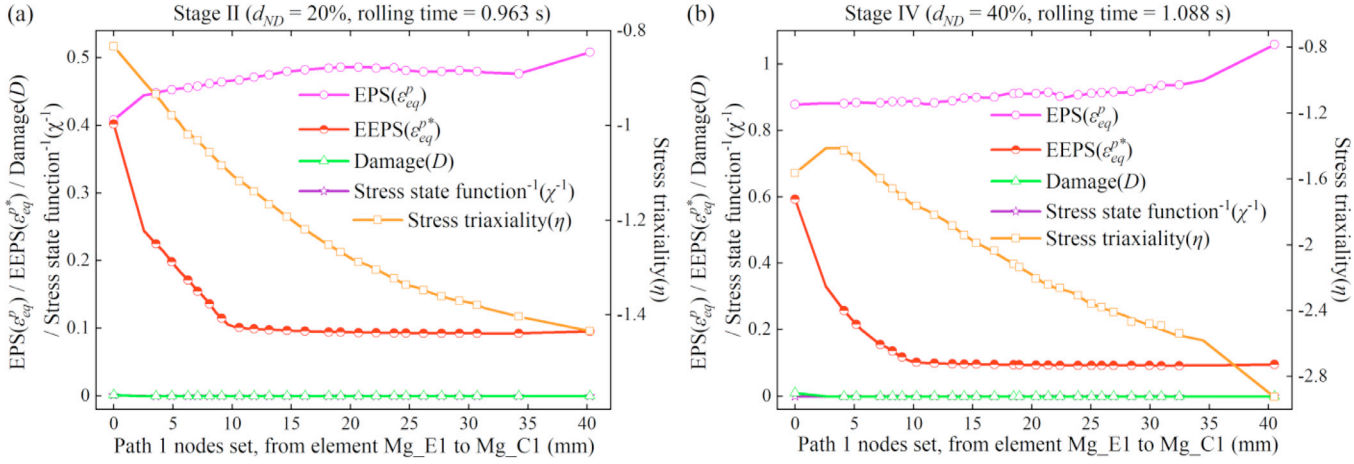

Fig. 6. The distribution of mechanical variables on the nodes set of Path 1 under proposed process, including EPS, EEPS, damage value, the reciprocal of the stress state function and stress triaxiality. (a) stage II (d_{ND} = 20%) and (b) stage IV (d_{ND} = 40%) correspond to the two stages of rolling according to the different deformation along the ND. Here, d_{ND} represents the deformation of the plate along ND at the position of element Mg_E1, and a clearer explanation can be obtained by referring to Fig. 3(a). Additionally, it should be noted that smaller reciprocal values of the stress state function indicate less propensity for damage accumulation. For further details on this variable, one can refer to previous research [34].

mogenization trend of EPS along the TD was observed across the entire plate surface. This phenomenon likely results from the constrained deformation of the Mg alloy along theTD due to the extrusion deformation of the Al alloy during the rolling process. Consequently, the metal's primary flow direction is predominantly in the RD, resulting in substantial plastic strain accumulation in this direction, which in turn elevates the EPS. In the context of damage evolution, it is evident that under the current deformation conditions, both the damage value and the reciprocal of the stress state function at the edge approach 0. This indicates that the proposed rolling process has altered the stress state at the plate's edge, thereby slowing the rate of damage evolution. By considering the distribution trend of the stress triaxiality, it is clear that the stress triaxiality at the edge of the Mg alloy is −0.83 during the proposed rolling process, which is significantly lower compared to the value of 0.027 under the conventional process at the same deformation level. The significant decrease in stress triaxiality weakens the cumulative rate of damage. Furthermore, although there is an accumulation of EPS at the edges of the Mg alloy, it is insufficient to cause a significant accumulation of damage values at lower rates. As the deformation of the plate along the ND increases to 40% (Fig. 6(b)), the accumulation of strain at the region near the Mg alloy edge (0 ∼ 30 mm) approaches uniformity, further improving the homogeneity of the plate. Besides, the difference between EPS and EEPS is further amplified, indicating that although the cumulative strain in EPS is significant, only a small portion of EPS transforms into EEPS, contributing to the evolution of damage. Furthermore, with further increase in deformation, the stress triaxiality at the edge of the plate further to decrease to −1.56. This is attributed to the downward pressure from the rolling mill, which intensifies the deformation of the Al alloy along the TD, thereby increasing the triaxial pressure at the plate's edge. The elevation in triaxial compressive stress mitigates the rate of damage evolution, effectively inhibiting the formation of edge cracks.

4.2. Examination of the edge stress state under the embedded composite rolling process

Fig. 7(a) illustrates the hydrostatic stress distribution in the Mg/Al composite plate under both rolling processes. In both processes, the hydrostatic stress progressively increases from the central to the edge regions of the composite plate. However, in the proposed process, the hydrostatic stress at the Mg alloy's edge is negative, indicating a significant volumetric compression during the plastic deformation process. To more clearly show the change trend of the two process stress states. The variation trends of the element Mg_E1′s hydrostatic and triaxial stresses on the Mg alloy edge during the proposed process are shown in Fig. 7(b). These variables exhibit a decreasing-then-increasing trend within the rolling zone. In terms of hydrostatic stress, the rolling zone's hydrostatic stress values are primarily negative because the edge Al alloy prevents the Mg alloy from deforming along the TD. Furthermore, during the time interval from 1.13 to 1.21 s, there was a further decrease in the stress triaxiality and hydrostatic stress of element Mg_E1. This is explained by the fact that the edge of Mg makes adequate contact with the Al alloy at this particular moment. The edge of the Mg alloy is under more pressure own to the strong deformation of the Al alloy. Consequently, during this time the Mg alloy's volumetric pressure reaches its maximum value.

To visually demonstrate the stress and deformation trends in the edge region of Mg alloy, a comparison of the stress states at different deformation stages (corresponding to d_{ND} =10% to 40%) for element Mg_E1 under two different processes is shown in Fig. 7(c). In Stage I, the triaxial stresses of element Mg_E1 are primarily in a compressive stress state due to the influence of Al alloy extrusion during the proposed rolling process. Particularly in the TD, it exhibits a significant compressive stress effect. However, in conventional rolling processes, the Mg alloy edge can deform freely along the TD. As a result, the element Mg_E1 experiences lower volumetric pressure. In stage II, the Mg alloy edge still experiences significant volumetric pressure, which hampers the rate of damage evolution. Conversely, during the conventional rolling process, the hydrostatic stress at the Mg alloy's edge remains positive. This is due to the relatively small restriction on the deformation freedom of the edge region. With the accumulation of plastic deformation, the primary deformation of the edge element no longer aligns parallel to the RD, but instead shifts towards the free end direction. Consequently, this leads to the further release of volumetric pressure and accelerates the process of internal voids expansion and coalescence within the matrix. With the further accumulation of deformation, the deformation along the TD of the Al alloy is intensified under the proposed rolling process, exerting greater pressure on the Mg alloy. As a result, the hydrostatic stress exhibits a decreasing trend. In contrast, under the conventional process, the hydrostatic stress remains positive, leading to a consistently high growth rate of damage.

The Lode parameter and the stress triaxiality serve as critical mechanical variables in the analysis of damage. The η - L space, constituted by these two variables, facilitates the visualization of stress states, thereby enhancing the distinction between compressive, tensile, and shear stress conditions. Fig. 7(d) illustrates a comparison of the element Mg_E1 in a two-dimensional η - L space for Mg/Al composite plate rolled using the proposed and conventional processes. In stage I, the numerical values of the Lode parameter for the Mg alloy edge are similar for both processes, and the stress states for both processes lie between pure shear and compression. However, under the proposed rolling process, the value of stress triaxiality is smaller, indicating a lower rate of damage accumulation. In stages II and III, under the conventional process, the element Mg_E1 is located at the free end of the plate. As the volumetric pressure progressively dissipates, the hydrostatic stress transitions from negative to positive, consequently elevating the stress triaxiality. In terms of the Lode parameter, the element's stress state progressively changes to pure shear during the current deformation stage, hastening the rate at which damage evolves. However, in the proposed rolling pro-

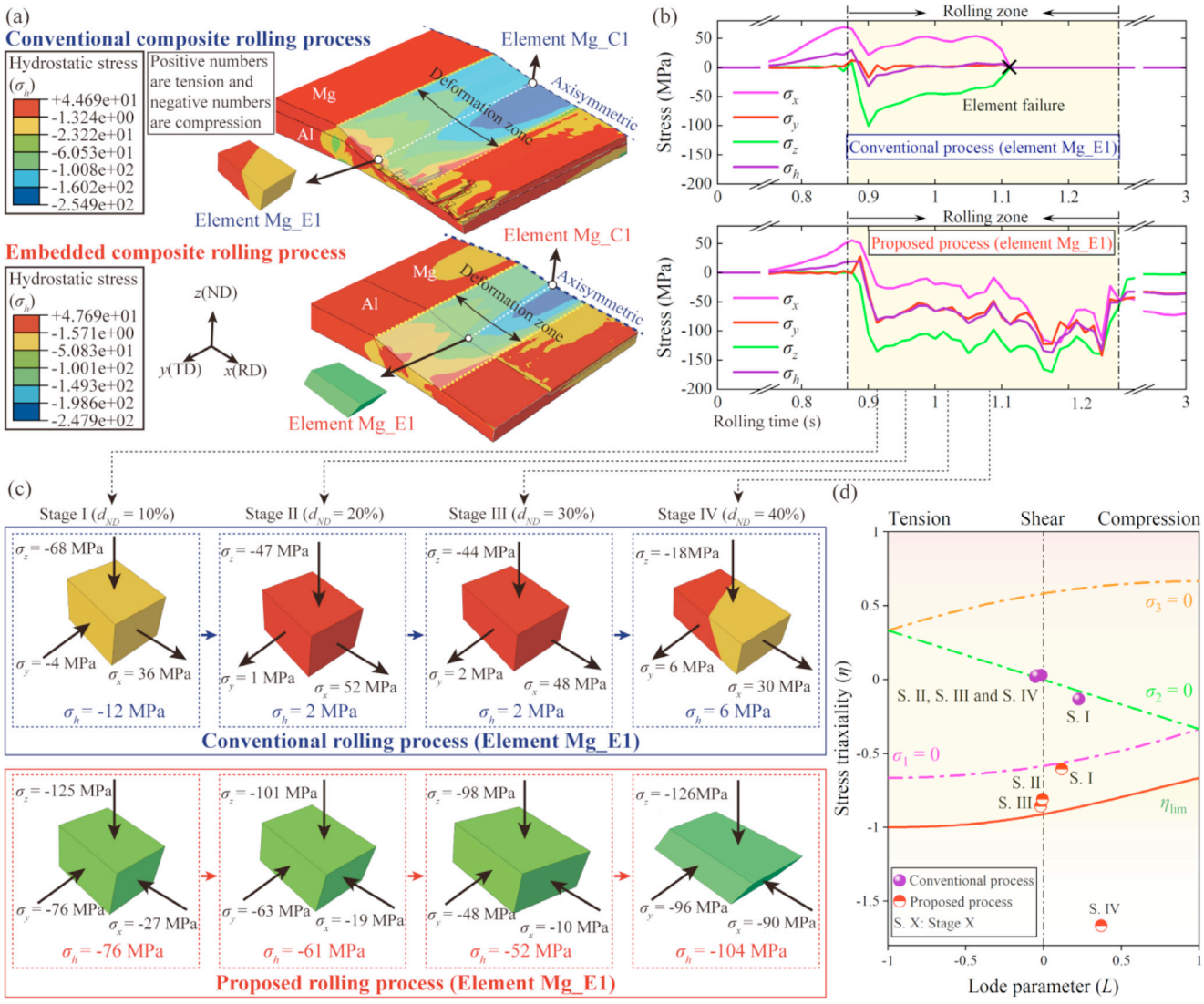

Fig. 7. Damage inhibition mechanism analysis during embedded composite rolling process. (a) Hydrostatic stress distribution on plate surface during rolling. (b) The element Mg_E1′s hydrostatic stress and triaxial stresses evolved with rolling time. (c) Deformation state of element Mg_E1 at different stages along the ND. (d) Comparison of the distribution of element Mg_E1 in (η–L) space at different deformation stages under both rolling processes.

cess, despite the Lode parameter of the element remains close to 0 (pure shear stress state), the deformation of the element is limited by the Al alloy. As a result, the hydrostatic stress further decreases (enhancing the volumetric pressure), leading to a further decrease of the stress triaxiality. This, in turn, results in a further suppression of cumulative damage. With the further increase in plate deformation, the stress state of the element under conventional process remains almost unchanged, consistently experiencing high stress triaxiality and pure shear stress. But in the proposed rolling process, as the deformation increases, the extrusion force that the Al alloy applies to the edge of the Mg alloy progressively increases, lead to a further decrease in the element's stress triaxiality. In stage IV, under the proposed process, the stress triaxiality of element Mg_E1 falls below the critical threshold. In this stress state, the conditions for damage evolution are no longer present, effectively inhibiting the generation of cracks.

5. Mechanical property evaluation

Bonding strength and tensile strength are crucial indicators for evaluating the forming performance of composite plates. This section compares the forming performance of plates at different positions under two processes and, through microstructural characterization, analyzes the differences in forming performance between the conventional and proposed processes.

To evaluate the forming quality of composite plates under both processes, shear and tensile specimens were sequentially extracted from the edge to the center of the rolled composite plates, as illustrated in Figs. 8(a) and (b). These specimens, designated as #S1 to #S4 for shear tests and #T1 to #T2 for tensile tests, were prepared for subsequent mechanical testing. The geometric dimensions of the shear and tensile specimens are depicted in Figs. 8(c) and (d), respectively. Notably, a

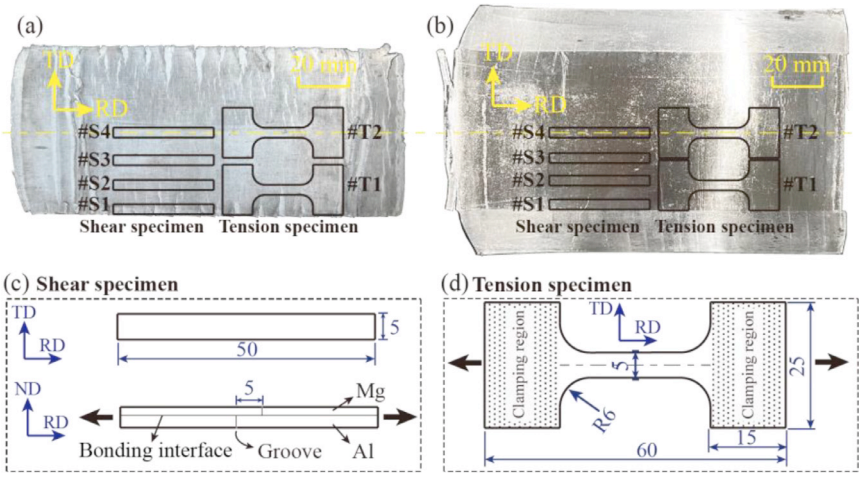

Fig. 8. The specimens' position at the plate and size in mechanical property test. The sampling position for shear and tensile tests conducted using conventional and proposed processes are illustrated in (a) and (b), respectively, with dimensions detailed in (c) and (d).

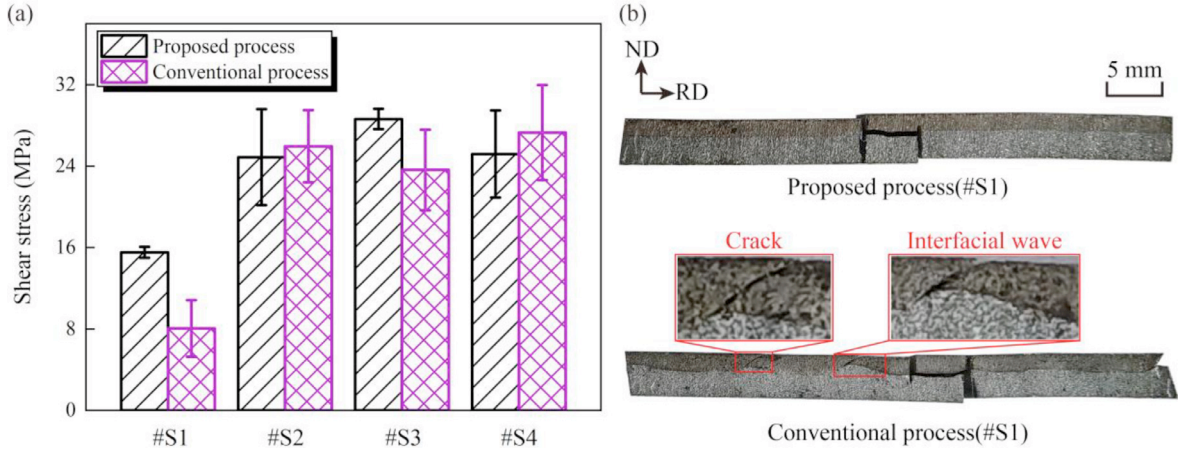

Fig. 9. The comparison of bonding strength rolled by two different processes, with a focus on the transition from edge to center, corresponding to shear specimens #S1 to #S4. Quantitative data comparisons are illustrated in (a), while macroscopic fracture morphology of the edge specimen #S1 is depicted in (b).

symmetrical slot with a length of 5 mm was made at the center of the shear specimens to facilitate the measurement of the bonding strength of the rolled plates. Furthermore, it is important to mention that the tensile and shear test specimens were extracted from identical locations on three different rolled composite plates. These mechanical experiments were repeated three times to minimize experimental error as much as possible.

5.1. Comparison of the bonding strength between the two processes

Fig. 9(a) illustrates the comparison of bond strength at various locations (from edge region #S1 to central region #S4) for Mg/Al laminated composites fabricated using two distinct rolling processes. It is observed that near the central positions #S2, #S3, and #S4, the bond strength of both processes is relatively similar, with the average bond strengths for the conventional and proposed processes being approximately 26 MPa and 27 MPa, respectively. At position #S1, closer to the edge of the plate, the bond strength of the conventional process is significantly lower, around 7 MPa. In contrast, the proposed process substantially enhances the bond strength at this location to approximately 16 MPa, which is about 2 times that of the conventional process. To elucidate the reasons behind this phenomenon, a comparison of the macroscopic morphology of edge specimens #S1 from both processes is presented in Fig. 9(b). The expansion of edge cracks in specimens prepared using conventional methods results in the evident presence of cracks and interface ripples on the end surfaces. These defects hinder adequate interface bonding, consequently leading to reduced bond strength. Conversely, the sample from the proposed process shows a uniform interface without evident cracks or defects, indicating a significant optimization of interface bonding quality and homogeneity.

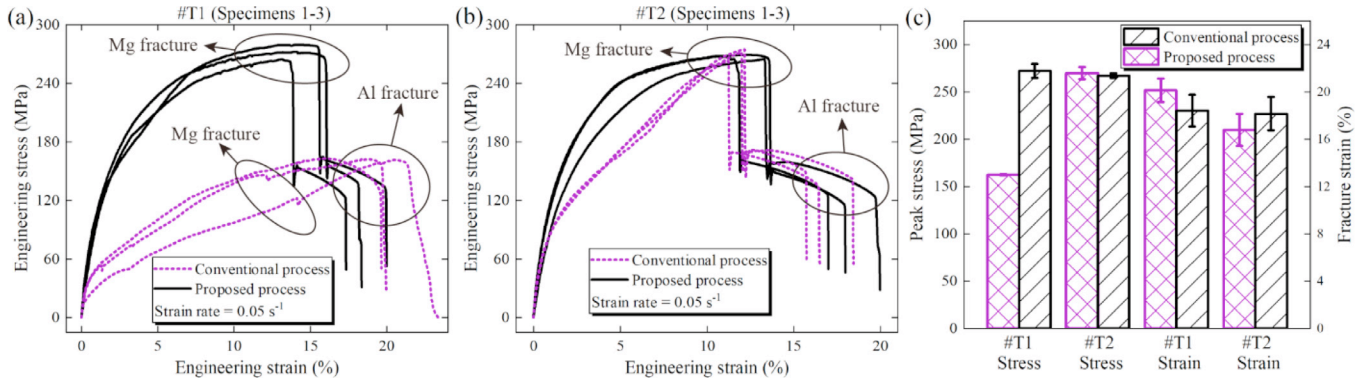

Fig. 10. The comparison of tensile properties under two different rolling techniques, including specimens from the edge region (#T1) and the center region (#T2). The mechanical curves for these two regions are compared in (a) and (b), respectively, with quantitative data comparisons provided in (c). It should be noted that thre e tests were conducted at each position to minimize experimental errors as much as possible. (For interpretation of the references to colour in this figure legend, the reader is referred to the web version of this article.)

5.2. Comparison of the tensile strength between the two processes

Figs. 10(a) and (b) illustrate the comparison of tensile strength between the edge and central regions of composite plates under different rolling processes. Own to the poor plasticity of Mg alloys compared to Al alloys at room temperature, Mg alloys fracture before Al alloys, resulting in two instances of stress reduction during mechanical loading. In the edge region of the plates (Fig. 10(a)), the loading curve under the conventional process exhibits a lower yield point and does not demonstrate a significant work hardening effect. Moreover, the magnitude of stress reduction caused by the fracture of Mg alloy is smaller, suggesting that defects might have already been present within the Mg alloy matrix before loading. In contrast, under the proposed process, the loading curve at the plate edges shows noticeable hardening, higher strength, and enhanced toughness, with smaller variations in repeated experiments. For the center region of the plates (Fig. 10(b)), the conventional process exhibits a lower yield point and a more linear plastic region on the curves, with less pronounced work hardening effect, indicating inferior toughness. This may be attributed to the differences in the internal microstructure of the materials due to the varying rolling processes. Fig. 10(c) presents a comparison of the average tensile strength and fracture strain at the edges and center of the rolled plates. For the edge region, the average peak strengths under the proposed and conventional processes are 272.3 MPa and 162.4 MPa, respectively, with the proposed process achieving a 67.7% improvement. For the central region, the average peak strengths are 269.9 MPa for the proposed process and 267.3 MPa for the conventional process, with average fracture strains of 18.17% and 16.8%, respectively. Although the strength under the conventional process is slightly higher, its fracture strain is reduced. A comparison of the mechanical properties at different locations within the same process reveals greater variability in the conventional process, whereas the proposed process exhibits stronger homogeneity along the TD. The reasons behind these phenomena will be discussed subsequently.

5.2.1. Analysis of the differences in tensile performance in the edge regions

To investigate the reasons behind the differences in the mechanical loading behavior of the edge regions of plates produced through various processes, Fig. 11 presents a comparison of the tensile properties of edge specimens from plates rolled using different techniques. Fig. 11(a) illustrates the morphology of the edge sample #T1 produced using conventional processes, where local stress softening due to crack propagation at the edges of the composite plate results in a wavy interface. Additionally, significant microcracks observed at the sample's end face, attributable to these initial defects, lead to rapid internal crack propagation within the Mg alloy during loading. This phenomenon prevents the Mg alloy from sustaining higher loads and reaching its forming limit prematurely, as depicted in Fig. 11(b), and is a primary reason for the material's inability to exhibit significant work hardening during the loading process. As the loading continues, the Al alloy also fractures, ultimately resulting in the complete loss of the material's load-bearing capacity. In contrast, the edge specimens of composite plates rolled using the proposed process, as shown in Fig. 11(d), are overall smooth and devoid of macroscopic cracks. During the loading process, both Mg and Al alloys are capable of undergoing effective plastic deformation and bearing loads, leading to more pronounced work hardening behavior. Consequently, this results in higher peak stress and improved toughness.

5.2.2. Analysis of the differences in tensile performance in the center regions

To investigate the differences in plastic strengthening within the central region of plates (#T2) under mechanical loading across various manufacturing processes, an analysis at a more microscopic level is necessary. Fig. 12 presents a comparative microscopic examination of the fracture surfaces

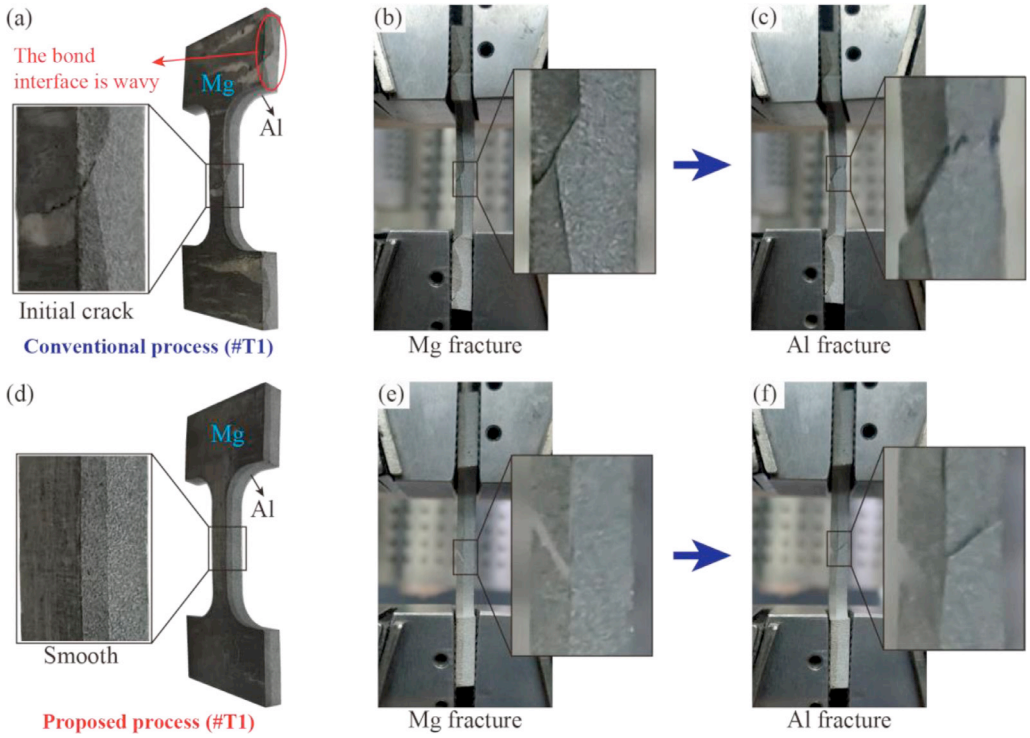

Fig. 11. The morphologies comparison of edge specimens #T1 rolled using two different processes, with initial specimens' comparisons shown in (a) and (d), corresponding to the conventional and proposed processes, respectively. Comparisons during the loading process are illustrated in (b) to (c) for the conventional process and (e) to (f) for the proposed process.

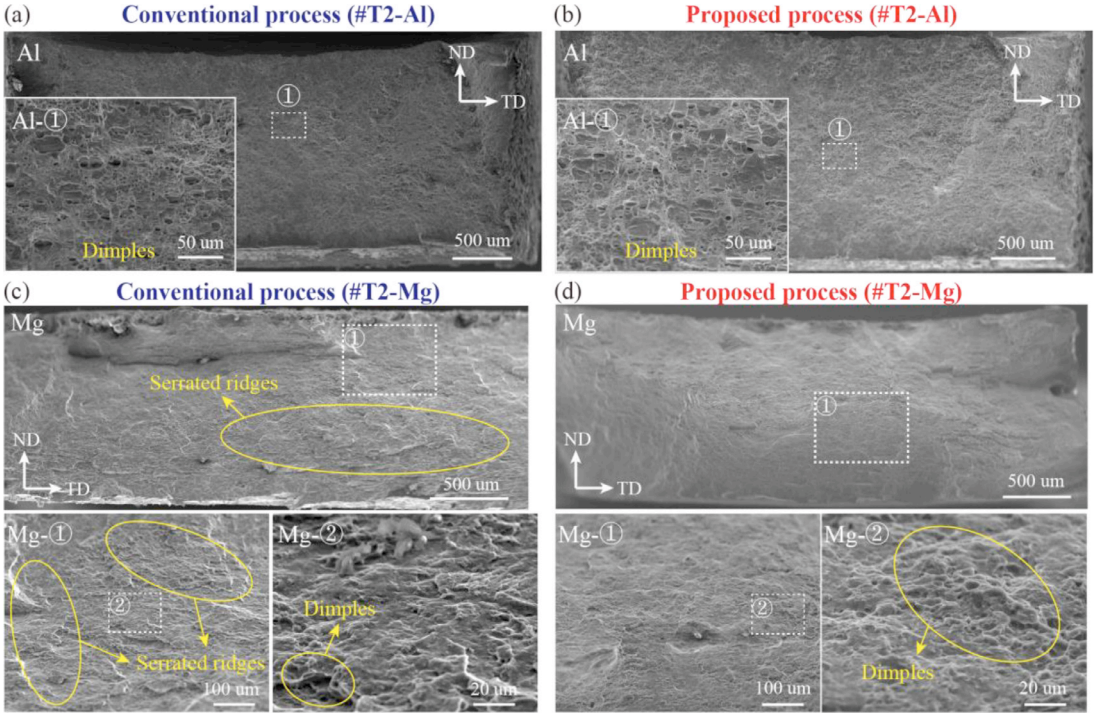

Fig. 12. The fracture morphologies comparison for specimens #T2 using two different processes. (a) and (c) correspond to the fracture surfaces of Al and Mg alloys, respectively, fabricated using the conventional process, while (b) and (d) correspond to those fabricated using the proposed process.

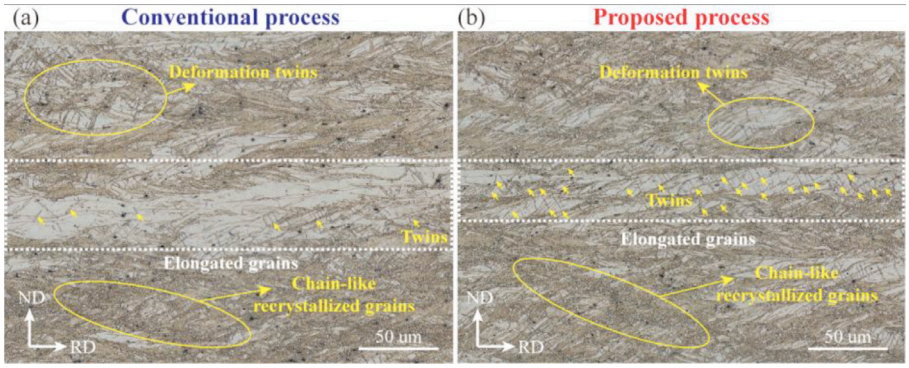

Fig. 13. The comparison of grain morphologies in the center region of plates rolled using two processes, with (a) and (b) corresponding to the conventional and proposed processes, respectively.

of tensile specimens from the central region of composite plates (#T2) processed through different techniques. For Al alloys (Figs. 12(a) and (b)), the fracture morphologies under both processes are similar, with a significant presence of uniform voids observed in the magnified images Al-① under both conditions, without the appearance of serrated tears. This indicates a uniformly ductile deformation mechanism in Al alloys under both processes. Given the similarity in fracture morphologies of Al alloys under both processes, the differences in plastic strengthening observed during mechanical loading are primarily attributed to the microstructural differences in Mg alloys. For Mg alloys (Figs. 12(c) and (d)), a significant number of serrated tears can be distinctly observed on the macroscopic fracture surfaces produced by conventional processes. These characteristics are more pronounced in the magnified images Mg-① and Mg-②, indicating the occurrence of uneven plastic flow and stress concentration during plastic deformation under conventional processing. Furthermore, the presence of unevenly distributed voids and dimples in Mg-② suggests a poor plastic response, reflecting a microstructure unfavorable for plastic deformation. Conversely, under the proposed process, the fracture surface exhibits a relatively smooth appearance with uniformly distributed dimples, as clearly observed in the magnified images Mg-① and Mg-②. The emergence of uniform equiaxed dimples indicates a ductile fracture mechanism through void coalescence under this process. Additionally, the absence of noticeable serrated tears under the proposed process suggests a more uniform local strain in Mg alloys during mechanical loading. Additionally, the absence of noticeable serrated tears under the proposed process suggests that the Mg layer has a more uniform local strain along the RD.

Fig. 13 illustrates a comparative analysis of the microstructural characteristics in the central regions of Mg plates fabricated using two different processes. The post-rolling microstructure of the Mg alloy, influenced by intense shear from the rolling process and DRX, exhibits a layered structure oriented along the ND. This structure comprises continuous fine recrystallized grains forming shear bands, severely deformed large grains, and a high density of deformation twins distributed within these grains [7]. The primary differences between the two processes are evident in the significantly elongated large grains along the RD. Under the proposed process, additional deformation constraints induce more intense plastic flow in the matrix metal along the RD. Consequently, the width of large grains in the Mg alloy is reduced in the proposed process compared to the conventional process, and there is a higher volume fraction of both layered and intersecting twins. Near the concentration areas, chain-like recrystallized grains are also observable. This suggests that the proposed process enhances the grain boundary density and promotes a more uniform microstructure in the Mg matrix compared to conventional rolling techniques. The crack nucleation and propagation trends shown in Fig. 12 are closely related to this. The main cause of brittle fracture is the instability of crack nucleation and propagation. In the composite plate manufactured by the traditional process, coarse grains and small grains are staggered in the Mg alloy. Since dislocations are easy to expand in coarse grains and are strongly hindered by dense grain boundaries in the aggregation area of small grains, the crack tips formed in the former will be blunted and delayed in expansion, while the latter will cause more serious stress concentration and lead to catastrophic cracks [44]. Therefore, ductile fracture and brittle fracture characteristics appear in different areas on the fracture. The plate prepared by the proposed process has a more uniform structure. Intuitively, the dimple size is small, and distribution are more widely distributed. The fracture morphologies presented in Figs. 12(a) and (b) further corroborate this, showing a less pronounced difference in the mixed fracture characteristics of the specimens produced by the proposed process, as opposed to the distinct zonal mixed fracture features observed in specimens from the conventional process.

To further elucidate the microstructural differences between two fabrication techniques, X-ray diffraction (XRD) was employed to statistically analyze the grain orientation in the central region of the plates. The pole figures of {0002} depicted in Figs. 14(a) and (b) reveal that, although the c-axes of some Mg alloy grains in both processes deviate towards the RD during rolling, the basal texture remains pronounced. Under the proposed process, the texture intensity in the central region of the plate increased by approximately 45.5% com-

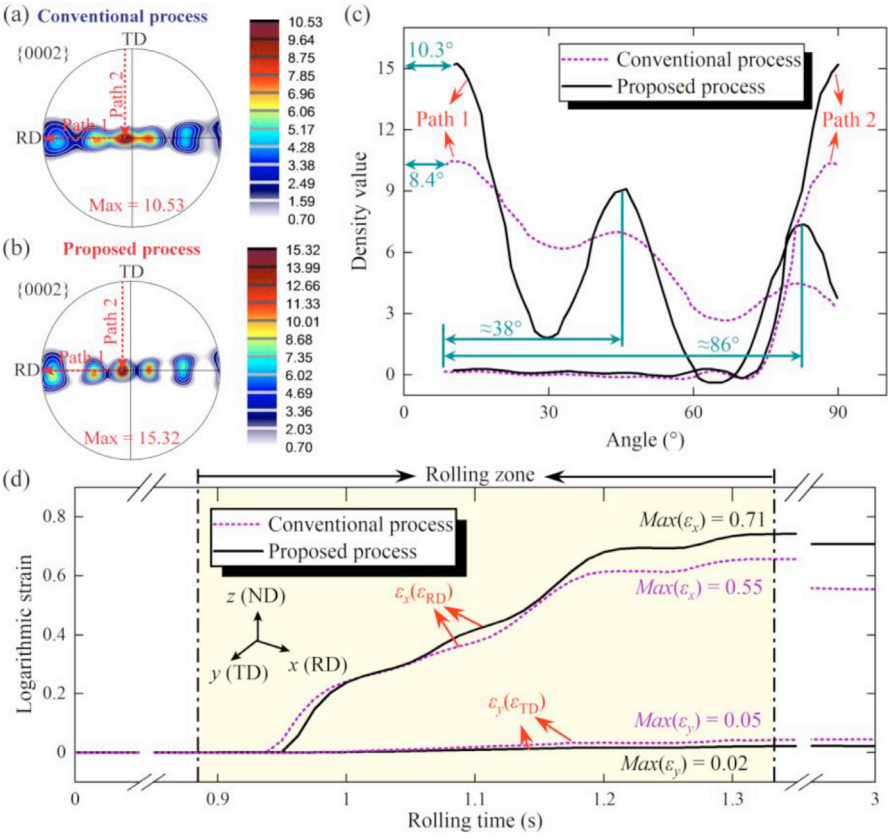

Fig. 14. The analysis of orientation differences in the central region of plates rolled using two different processes. The comparison of {0002} pole density is depicted in (a) and (b), respectively, while (c) demonstrates the quantified trends of pole density variation at Path 1 and 2 with angle for both processes. The trend of strain variation for the element Mg_C1 in the central region of plates under two different techniques, along the RD and TD, is depicted in (d). (the position of element Mg_C1 at the plate can be referenced in Fig. 7(a)).

pared to the conventional process. Along paths 1 and 2 set in the RD and TD directions on the pole figures, the density values of the ⟨0002⟩ pole axis as a function of the deviation angle are shown in Fig 14(c). The distribution curves indicate that the influence on the RD post-rolling is more pronounced in both processes, indirectly demonstrating that, compared to conventional process, the proposed process not only mitigates cracking but also enhances the unidirectional plastic deformation of Mg alloy. Simulation results vividly illustrate this process. As shown in Fig 14(d), the maximum strain in the element Mg_C1 in the central region of the plate along the RD is 0.71 under the proposed process, compared to only 0.55 in the conventional process. The maximum strain along the TD direction is 0.02 in the proposed process, whereas it reaches 0.05 in the conventional process. The proposed technique restricts plastic flow along the TD and intensifies the overall plastic flow trend along the RD, implying that the freedom of grain rotation is constrained, thereby promoting the deviation of the {0002} basal plane towards the rolling plane and forming a stronger basal texture. Notably, the density distribution of the pole axis forms peaks near 38° and 86°. According to previous reports, these specific orientations are primarily due to the activation of prismatic slip ⟨a⟩ and pyramidal slip $\langle c + a \rangle$ during the hot rolling of Mg alloys, as well as the occurrence of {10–11}-{10–12} double twins and {10–12} extension twins [45].

The microstructural characteristics directly influence the tensile properties of Mg alloy layers, thereby affecting the overall strength and toughness of composite plates fabricated using two different processes. During tensile testing along the RD, the basal planes of the Mg alloy exhibit a deviation from the ideal orientation, with the c-axis tilting. When the majority of the Mg alloy grains have a basal plane angle of less than 13° relative to the RD-TD plane, prismatic slip on the a-axis becomes dominant [46,47]. The proposed process enhances the basal texture strength significantly, increasing the contribution of prismatic slip during deformation. In contrast, the conventional process tends to facilitate basal slip on the c-axis, which is more readily activated. This suggests that composite plates produced by the proposed process demonstrate more pronounced work hardening and a more stable hardening rate in the early stages of plastic deformation. Overall, the dual reinforcement mechanism, resulting from a higher density of grain boundaries and stronger basal texture, endows the composite plates manufactured using the proposed process with a notably enhanced work hardening effect and improved toughness compared to those produced by the conventional process.

5. Conclusion

This study introduces a novel rolling process, called 'embedded composite rolling,' designed to mitigate edge cracking in Mg alloys by embedding them within Al alloys during the Mg/Al composite plate rolling process. The enhanced Lemaitre model simulation was employed to reveal the cause by which this proposed process suppresses edge defects. Furthermore, this paper conducts a comparative analysis of the mechanical properties of plates rolled using both rolling processes. The primary conclusions drawn from this study are outlined below:

1. A novel 'embedded composite rolling' technique, developed through the grooving treatment of Al alloys, has been proposed to inhibit edge defects in Mg/Al composite plates during rolling. The comparative validation between the proposed process and the conventional process was conducted at 350 °C with a 50% reduction rate. The results indicated that the plates rolled using the proposed process exhibited a smooth and even surface, with no macroscopic edge cracks detected. Furthermore, the side interface of the plates was straight, in stark contrast to the wavy interface observed in plates produced by the conventional process, signifying a notable improvement in the forming quality of the plates.
2. Utilizing an enhanced Lemaitre damage model, the evolution of damage in the composite plate under two different processes was assessed. The findings indicate that the maximum edge damage prediction for the proposed process decreased by 96% compared to the conventional process. This significant reduction can be attributed to the following factors: during the rolling process of the proposed technique, the Al alloy restricts the deformation of the Mg alloy along the TD. This restriction, on one hand, promotes the metal flow of Mg alloy along the RD at the edges, leading to more uniform deformation and effectively preventing stress concentration. On the other hand, the deformation of the Al alloy provides substantial support to the edges of the Mg alloy, inducing a triaxial compressive stress state. The elevated triaxial compressive stress leads to a reduction in edge stress triaxiality ($\eta_{\max}$ from -0.02 to -1.56), which falls below the critical stress triaxiality threshold, thereby preventing the evolution of damage.
3. The comparison of the mechanical properties of rolled plates produced by two different processes revealed that the proposed method significantly enhances the homogeneity along the TD and the mechanical performance in the edge regions of the plates. Specifically, the edge bonding strength and tensile strength of the plates processed by the proposed method exhibited increases of 118% and 68%, respectively, compared to those produced using conventional rolling techniques. Furthermore, the rolled plates produced by the proposed process exhibit enhanced toughness. This phenomenon can be attributed to the restriction of plastic flow along the TD and the reinforcement of plastic flow along the RD, resulting in a higher density of grain boundaries and a stronger basal texture.

Declaration of competing interest

The authors declare that they have no known competing financial interests or personal relationships that could have appeared to influence the work reported in this paper.

CRediT authorship contribution statement

Chenchen Zhao: Writing – original draft, Software, Methodology, Conceptualization. **Zhiquan Huang:** Methodology, Conceptualization. **Haoran Zhang:** Writing – review & editing, Methodology. **Peng Li:** Methodology, Data curation. **Tao Wang:** Writing – review & editing, Supervision, Funding acquisition, Conceptualization. **Qingxue Huang:** Project administration, Funding acquisition.

Acknowledgment

This work was supported by National Key Research and Development Program (2018YFA0707300); Major Program of National Natural Science Foundation of China (U22A20188).

Appendix A. Numerical implementation method of the enhanced Lemaitre damage model

Step 1: Calculate trial stress and update internal variable.

To avoid the loss of variables in the calculation process, these variables need to be updated in the Step 1, and the test stress need to be calculated (assuming the current increment step is elastic). The related equations are as follows:

$$\text{Calculate}: \begin{cases} \text{trial stress tensor}: (\sigma_{ij})_{n+1}^{trial} = (\sigma_{ij})_n + \mathbf{C} : \Delta\varepsilon_{ij}^{e} \\ \text{trial hydrostatic stress}: (\sigma_h)_{n+1}^{trial} = Tr[(\sigma_{ij})_{n+1}^{trial}]/3 \\ \text{the second invariant of deviational stress}: \\ \quad J_2 = \frac{1}{2}(s_{ij})_{n+1}^{trial}(s_{ij})_{n+1}^{trial} \\ \text{the third invariant of deviational stress}: J_3 = \det(\mathbf{s}) \\ \text{trial von}-\text{Mises stress}: (\sigma_{eq})_{n+1}^{trial} = \sqrt{3J_2} \end{cases} \tag{A.1}$$

$$\text{Update}: \begin{cases} (\varepsilon_{ij}^{p})_{n+1} = (\varepsilon_{ij}^{p})_n \\ (\varepsilon_{eq}^{p})_{n+1} = (\varepsilon_{eq}^{p})_n \\ (D)_{n+1} = (D)_n \end{cases} \tag{A.2}$$

Step 2: Calculate the variables required for stress state function.

$$\text{Calculate}: \begin{cases} \text{Lodeangle}: \theta_L = \frac{1}{3}\sin^{-1}[\frac{-\sqrt{27}J_3}{2(J_2)^{3/2}}] \\ \text{Lodeparameter}: L = \sqrt{3}\tan\theta_L \\ \text{stresstriaxiality}: \eta = \frac{(\sigma_h)_{n+1}^{trial}}{(\sigma_{eq})_{n+1}^{trial}} \end{cases} \tag{A.3}$$

Step 3: Assess whether plastic conditions are met.

Set $(*)_{n+1} = (*)_{n+1}^{trial}$, and calculate the yield surface equation of damage model:

$$\Phi = (\sigma_y)_{n+1} - [1 - (D)_{n+1}](\sigma_{eq})_{n+1}. \tag{A.4}$$

Proceed to Step 4 if the yield condition is met, or Step 5 if Eq. (A.4) ≥ 0.

Step 4: Solving the equivalent plastic strain increment by Newton-Raphson algorithm.

Decide on the starting EPS increment value (iterative step $i = 1$) $(\Delta\varepsilon_{eq}^{p})^{i}$=0.

Calculate the partial derivative of the potential function.

$$f(\Delta\varepsilon_{eq}^{p}) = \frac{\partial\Phi}{\partial\Delta\varepsilon_{eq}^{p}} = \frac{\partial\Phi}{\partial\sigma_y}\frac{\partial\sigma_y}{\partial\Delta\varepsilon_{eq}^{p}} + \frac{\partial\Phi}{\partial\dot{D}}\frac{\partial\dot{D}}{\partial\Delta\varepsilon_{eq}^{p}} + \frac{\partial\Phi}{\partial\sigma_{eq}}\frac{\partial\sigma_{eq}}{\partial\Delta\varepsilon_{eq}^{p}}, \tag{A.5}$$

where the derivation details are summarized in Appendix B.

Update variables.

$$\text{Update}: \begin{cases} (\Delta\varepsilon_{eq}^{p})^{i+1} = (\Delta\varepsilon_{eq}^{p})^{i} - \frac{\Phi[(\Delta\varepsilon_{eq}^{p})^{i}]}{f[(\Delta\varepsilon_{eq}^{p})^{i}]} \\ (\varepsilon_{eq}^{p})_{n+1}^{i+1} = (\varepsilon_{eq}^{p})_{n+1} + (\Delta\varepsilon_{eq}^{p})^{i+1} \\ (\sigma_y)_{n+1}^{i+1} = (\sigma_y)_{n+1} + \frac{\partial(\sigma_y)_{n+1}}{\partial\Delta\varepsilon_{eq}^{p}}(\Delta\varepsilon_{eq}^{p})^{i+1}, \\ (D)_{n+1}^{i+1} = (D)_{n+1} + \frac{\partial(D)_{n+1}}{\partial\Delta\varepsilon_{eq}^{p}}(\Delta D)_{n+1}^{i+1} \\ (\sigma_{eq})_{n+1}^{i+1} = (\sigma_{eq})_{n+1} - 3G(\Delta\varepsilon_{eq}^{p})^{i+1} \end{cases} \tag{A.6}$$

where $G = \frac{E}{2(1+\mu)}$ is the shear modulus (μ and E are poisson ratio and young modulus of materials, respectively).

Cyclic calculate the Eq. (A.5) and Eq. (A.6) until the Eq. (A.4) meets the termination condition, and then go to Step 5.

Step 5: Determine whether the element has reached the failure condition.

If damage value $D \geq 1$, then remove this element and jump to Step 7, else continue to Step 6.

Step 6: Update the stress and plastic strain tensors.

Set $(*)_{n+1} = (*)_{n+1}^{i}$.

Calculate the stress tensor.

$$(s_{ij})_{n+1} = (s_{ij})_{n+1}^{trial} - 2G\Delta\varepsilon_{eq}^{p}. \tag{A.7}$$

Calculate the plastic strain tensor.

$$(\varepsilon_{ij}^{p})_{n+1} = \frac{3(s_{ij})_{n+1}(\varepsilon_{eq}^{p})_{n+1}}{2(\sigma_{eq})_{n+1}}. \tag{A.8}$$

Step 7: Proceed to the next incremental step.

Set $(^{*})_{n+2} = (^{*})_{n+1}$.

Appendix B. A summary of the derivative details

1. Flow stress model

This study employs a flow stress model that incorporates DRX, detailed in Section 3. The equation is as follows:

$$\begin{aligned}\sigma_y &= \left[\sigma_s^2 + \left(\sigma_0^2 - \sigma_s^2\right)\exp\left(-\Omega_\varepsilon\varepsilon_{eq}^{p}\right)\right]^{1/2} - (\sigma_s - \sigma_{ss})X_{drx}X_{drx} \\ &= \left[1 + k_v \wedge \left(1 - \frac{\varepsilon_p^{eq} - \varepsilon_c}{\varepsilon_{0.5} - \varepsilon_c}\right)\right]^{-1}.\end{aligned} \tag{B.1}$$

The derivation details of Eq. (B.1) are as follows:

$$\frac{\partial\Phi}{\partial\sigma_y} = 1 \tag{B.2}$$

$$\begin{aligned}\frac{\partial\sigma_y}{\partial\Delta\varepsilon_{eq}^{p}} &= -\frac{\Omega_\varepsilon\exp\left(-\Omega_\varepsilon\varepsilon_{eq}^{p}\right)\left(\sigma_0^2 - \sigma_s^2\right)}{2\sqrt{\sigma_s^2 + \left(\sigma_0^2 - \sigma_s^2\right)\exp\left(-\Omega_\varepsilon\varepsilon_{eq}^{p}\right)}} \\ &\quad - (\sigma_s - \sigma_{ss})\frac{\partial X_{DRX}}{\partial\Delta\varepsilon_{eq}^{p}} \\ \frac{\partial X_{DRX}}{\partial\Delta\varepsilon_{eq}^{p}} &= \frac{k_v \wedge \left(1 - \frac{\varepsilon_p^{eq} - \varepsilon_c}{\varepsilon_{0.5} - \varepsilon_c}\right)\ln(k_v)(\sigma_s - \sigma_{ss})}{\left[k_v \wedge \left(1 - \frac{\varepsilon_p^{eq} - \varepsilon_c}{\varepsilon_{0.5} - \varepsilon_c}\right) + 1\right]^2(\varepsilon_{0.5} - \varepsilon_c)},\end{aligned} \tag{B.3}$$

where ε_{eq}^{p} is the value of the $i+1$ iteration step, which contains the EPS increment $\Delta\varepsilon_{eq}^{p}$, that is, $(\varepsilon_{eq}^{p})_{n+1}^{i+1} = (\varepsilon_{eq}^{p})_{n+1} + (\Delta\varepsilon_{eq}^{p})^{i+1}$.

2. Damage

$$\frac{\partial\Phi}{\partial\dot{D}} = \sigma_{eq} \tag{B.4}$$

$$\frac{\partial\dot{D}}{\partial\Delta\varepsilon_{eq}^{p}} = n(\varepsilon_{eq}^{p*})^{n-1}(\varepsilon_f)^{-n} + n(n-1)(\varepsilon_{eq}^{p*})^{n-2}(\varepsilon_f)^{-n}\dot{\varepsilon}_{eq}^{p}, \tag{B.5}$$

where ε_{eq}^{p*} also represents the value of the $i+1$ iteration step, and its incremental form is as follows:

$$\begin{aligned}(\varepsilon_{eq}^{p*})_{n+1}^{i+1} &= (\varepsilon_{eq}^{p*})_{n+1} + (\Delta\varepsilon_{eq}^{p})^{i+1} \text{for} \eta > \eta_{\lim} \\ (\varepsilon_{eq}^{p*})_{n+1}^{i+1} &= (\varepsilon_{eq}^{p*})_{n+1} + 0 \text{for} \eta < \eta_{\lim}.\end{aligned} \tag{B.6}$$

3. von-Mises equivalent stress

$$\frac{\partial\Phi}{\partial\sigma_{eq}} = D \tag{B.7}$$

$$\frac{\partial\sigma_{eq}}{\partial\Delta\varepsilon_{eq}^{p}} = -3G, \tag{B.8}$$

where the incremental form of σ_{eq} is $(\sigma_{eq})_{n+1}^{i+1} = (\sigma_{eq})_{n+1} - 3G(\Delta\varepsilon_{eq}^{p})^{i+1}$.

References

[1] Y. Wang, M. Tayyebi, M. Tayebi, M. Yarigarravesh, S. Liu, H. Zhang, J Magnes Alloys 11 (2023) 966–980, doi:10.1016/j.jma.2022.11.004.

[2] M. Huang, C. Xu, G. Fan, E. Maawad, W. Gan, L. Geng, F. Lin, G. Tang, H. Wu, Y. Du, D. Li, K. Miao, T. Zhang, X. Yang, Y. Xia, G. Cao, H. Kang, T. Wang, T. Xiao, H. Xie, Acta Mater 153 (2018) 235–249, doi:10.1016/j.actamat.2018.05.005.

[3] S. Li, Z. Chu, H. Gui, L. Tuo, J. Han, T. Wang, Q. Huang, J Mat Res Technol 26 (2023) 2695–2710, doi:10.1016/j.jmrt.2023.08.053.

[4] G. Li, W. Jiang, F. Guan, Z. Zhang, J. Wang, Y. Yu, Z. Fan, J Magnes Alloys 11 (2023) 3059–3098, doi:10.1016/j.jma.2023.09.001.

[5] F. Guan, W. Jiang, G. Li, J. Zhu, J. Wang, G. Jie, Z. Fan, J Magnes Alloys 10 (2022) 2296–2309, doi:10.1016/j.jma.2021.11.023.

[6] M. Acarer, B. Demir, B. Dikici, E. Salur, J Magnes Alloys 10 (2022) 1086–1095, doi:10.1016/j.jma.2021.08.009.

[7] H. Jia, S. Jiang, J. Han, S. Cao, T. Wang, Q. Huang, Mater Sci Eng A 870 (2023) 144903, doi:10.1016/j.msea.2023.144903.
[8] T. Liu, B. Song, G. Huang, X. Jiang, S. Guo, K. Zheng, F. Pan, J Magnes Alloys 10 (2022) 2062–2093, doi:10.1016/j.jma.2022.08.001.
[9] Y. Xu, W. Jiang, Q. Li, Y. Niu, L. Yu, G. Li, Z. Fan, J Mat Res Technol 30 (2024) 6870–6876, doi:10.1016/j.jmrt.2024.05.097.
[10] Q. Liu, B. Feng, H. Yang, J. Song, B. Xiao, B. Jiang, L. Wu, Q. Shen, K. Zheng, F. Pan, J Mat Res Technol 19 (2022) 5037–5048, doi:10.1016/j.jmrt.2022.07.022.
[11] T. Wang, Y. Wang, L. Bian, Q. Huang, Mater Sci Eng A 765 (2019) 138318, doi:10.1016/j.msea.2019.138318.
[12] J. Lei, L. Ma, Z. Cai, W. Jia, Y. Yuan, H. Pan, H. Xie, J Magnes Alloys 12 (2023) 4244–4258, doi:10.1016/j.jma.2023.04.012.
[13] N.A. Muhammad, P. Geng, C. Wu, N. Ma, Int J Mach Tools Manuf 186 (2023) 104004, doi:10.1016/j.ijmachtools.2023.104004.
[14] X. Ma, P. Li, T. Wang, Z. Ren, P. Chen, J. Ji, J Magnes Alloys (2024) S2213956724002160, doi:10.1016/j.jma.2024.06.013.
[15] S. Zhang, Y. Ruan, X. Han, L. Hu, M. Li, Q. He, T. Zhou, L. Shi, S. Jiang, Mater Today Commun 33 (2022) 104573, doi:10.1016/j.mtcomm.2022.104573.
[16] X. Rao, Y. Wu, X. Pei, Y. Jing, L. Luo, Y. Liu, J. Lu, Mat Sci Engineer A 754 (2019) 112–120, doi:10.1016/j.msea.2019.03.047.
[17] C. Zhi, L. Ma, Q. Huang, Z. Huang, J. Lin, J Mat Process Technol 255 (2018) 333–339, doi:10.1016/j.jmatprotec.2017.12.022.
[18] B. Li, B. Teng, E. Wang, Mat Sci Engineer A 765 (2019) 138317, doi:10.1016/j.msea.2019.138317.
[19] W. Jia, Q. Le, Y. Tang, Y. Ding, F. Ning, J. Cui, J Mater Sci Technol 34 (2018) 2069–2083, doi:10.1016/j.jmst.2018.04.005.
[20] J. Tian, H. Lu, W. Zhang, H. Nie, Q. Shi, J. Deng, W. Liang, L. Wang, J Magnes Alloys 10 (2022) 2193–2207, doi:10.1016/j.jma.2021.01.007.
[21] J. Luo, H. Yan, L.W. Lu, R.S. Chen, A.R. Wu, F.C. Yin, J Alloys Compd 883 (2021) 160813, doi:10.1016/j.jallcom.2021.160813.
[22] Z. Huang, Q. Huang, J. Wei, L. Ma, D. Wu, D. He, J Mater Process Technol 246 (2017) 85–92, doi:10.1016/j.jmatprotec.2017.01.034.
[23] C. Zhao, T. Wang, Z. Li, J. Liu, Z. Huang, Q. Huang, Int J Mech Sci 241 (2023) 107961, doi:10.1016/j.ijmecsci.2022.107961.
[24] H. Wu, Q. Qian, W. Xu, C. Liu, J. Xu, D. Shan, B. Guo, J Mat Res Technol 30 (2024) 1594–1610, doi:10.1016/j.jmrt.2024.03.131.
[25] Z. Pater, J. Tomczak, T. Bulzak, Ł. Wójcik, M.M. Skripalenko, Int J Mach Tool Manufact 163 (2021) 103706, doi:10.1016/j.ijmachtools.2021.103706.
[26] X. Zhou, Z. Shao, C. Zhang, F. Sun, W. Zhou, L. Hua, J. Jiang, L. Wang, Int J Mach Tools Manuf 159 (2020) 103647, doi:10.1016/j.ijmachtools.2020.103647.
[27] W. Xu, H. Wu, H. Ma, D. Shan, Int J Mech Sci 135 (2018) 226–239, doi:10.1016/j.ijmecsci.2017.11.024.
[28] L. Niu, Q. Zhang, Y. Ma, Y. Chen, B. Han, K. Huang, Int J Plast 149 (2022) 103185, doi:10.1016/j.ijplas.2021.103185.
[29] J. Lemaitre, J Eng Mater Technol-Trans ASME 107 (1985) 83–89, doi:10.1115/1.3225775.
[30] A.L. Gurson, Continuum theory of ductile rupture by void nucleation and growth. Part I. Yield criteria and flow rules for porous ductile media, J Eng Mater Technol 99 (1975) 297–300, doi:10.2172/7351470.
[31] Z. He, H. Zhu, Y. Hu, Int J Mech Sci 192 (2021) 106081, doi:10.1016/j.ijmecsci.2020.106081.
[32] H. Wu, X. Zhuang, Z. Zhao, Int J Solid Struct 239–240 (2022) 111452, doi:10.1016/j.ijsolstr.2022.111452.
[33] X. Chen, Y. Du, K. Du, N. Xiang, Z. Li, X. Tian, M. Liu, Eng Fract Mech 273 (2022) 108711, doi:10.1016/j.engfracmech.2022.108711.
[34] T. Wang, C. Zhao, G. Zhang, W. Zhao, Q. Huang, Composit Part B: Engineer 275 (2024) 111347, doi:10.1016/j.compositesb.2024.111347.
[35] J. Zhou, X. Gao, J.C. Sobotka, B.A. Webler, B.V. Cockeram, Int J Solid Struct 51 (2014) 3273–3291, doi:10.1016/j.ijsolstr.2014.05.028.
[36] Y. Lou, J.W. Yoon, H. Huh, Int J Plast 54 (2014) 56–80.
[37] N. Aravas, Int J Numer Meth Engng 24 (1987) 1395–1416, doi:10.1002/nme.1620240713.
[38] S. Wang, Z. Chen, C. Dong, Int J Mech Sci 133 (2017) 288–302, doi:10.1016/j.ijmecsci.2017.08.028.
[39] A. Shterenlikht, N.A. Alexander, Comput Method Appl Mech Eng 237–240 (2012) 1–9, doi:10.1016/j.cma.2012.04.018.
[40] S. Serajzadeh, A.Karimi Taheri, Mech Res Commun 30 (2003) 87–93, doi:10.1016/S0093-6413(02)00354-3.
[41] X. Shang, Z. Cui, M.W. Fu, Int J Plast 95 (2017) 105–122, doi:10.1016/j.ijplas.2017.04.002.
[42] J. Liu, Z. Cui, L. Ruan, Mat Sci Engineer A 529 (2011) 300–310, doi:10.1016/j.msea.2011.09.032.
[43] S.W. Chen, P.F. Gao, M. Zhan, F. Ma, H.R. Zhang, R.Q. Xu, J Mat Process Technol 265 (2019) 44–55, doi:10.1016/j.jmatprotec.2018.10.003.
[44] I.A. Ovid'ko, R.Z. Valiev, Y.T. Zhu, Prog Mater Sci 94 (2018) 462–540, doi:10.1016/j.pmatsci.2018.02.002.
[45] J.H. Lee, J.U. Lee, S.-H. Kim, S.W. Song, C.S. Lee, S.H. Park, J Mater Sci Technol 34 (2018) 1747–1755, doi:10.1016/j.jmst.2018.03.002.
[46] H. Yu, C. Li, Y. Xin, A. Chapuis, X. Huang, Q. Liu, Acta Mater 128 (2017) 313–326, doi:10.1016/j.actamat.2017.02.044.
[47] H. Yu, Y. Xin, Y. Cheng, B. Guan, M. Wang, Q. Liu, Mater Sci Eng A 700 (2017) 695–700, doi:10.1016/j.msea.2017.06.034.